

Reconstructing the direction of reactor antineutrinos via electron scattering in Gd-doped water Cherenkov detectors

D. Hellfeld,^{1,*} S. Dazeley,^{2,†} A. Bernstein,² and C. Marianno¹

¹*Department of Nuclear Engineering, Texas A&M University, College Station, TX 77843*

²*Lawrence Livermore National Laboratory, Livermore, CA 94550*

(Dated: December 4, 2015)

The potential of elastic antineutrino-electron scattering ($\bar{\nu}_e + e^- \rightarrow \bar{\nu}_e + e^-$) in a Gd-doped water Cherenkov detector to determine the direction of a nuclear reactor antineutrino flux was investigated using the recently proposed WATCHMAN antineutrino experiment as a baseline model. The expected scattering rate was determined assuming a 13 km standoff from a 3.758 GWt light water nuclear reactor. Background was estimated via independent simulations and by appropriately scaling published measurements from similar detectors. Many potential backgrounds were considered, including solar neutrinos, misidentified reactor-based inverse beta decay interactions, cosmogenic radionuclide and water-borne radon decays, and gamma rays from the photomultiplier tubes, detector walls, and surrounding rock. The detector response was modeled using a GEANT4-based simulation package. The results indicate that with the use of low radioactivity PMTs and sufficient fiducialization, water-borne radon and cosmogenic radionuclides pose the largest threats to sensitivity. The directional sensitivity was then analyzed as a function of radon contamination, detector depth, and detector size. The results provide a list of theoretical conditions that, if satisfied in practice, would enable nuclear reactor antineutrino directionality in a Gd-doped water Cherenkov detector approximately 10 km from a large power reactor.

Keywords: Nuclear reactor antineutrinos, Water Cherenkov detector, Electron scattering, Directionality

I. INTRODUCTION

Near-field (< 100 m) monitoring of nuclear reactors via measurements of the antineutrino flux and energy spectrum has been demonstrated using cubic meter scale liquid scintillator antineutrino detectors such as [1–3]. With such measurements, reactor characteristics such as the operational status (on/off), relative power output, and the evolution of the fissionable isotopes in the fuel (burnup) could be determined. The success of these detectors has spurred research in much larger detectors in order to increase both sensitivity and standoff distance [4, 5]. Such detectors could potentially be used as a tool in the nuclear safeguards regime set forth by the International Atomic Energy Agency (IAEA) to reduce the effort needed to conduct physical inspections inside of declared reactor facilities, to monitor facilities in which inspectors do not have access, or to either exclude or search for the presence of clandestine reactors in suspected locations.

Kiloton and megaton scale Gd-doped water Cherenkov antineutrino detectors (WCDs), such as the recently proposed WATER Cherenkov Monitor of ANtineutrinos (WATCHMAN) project [6], are being investigated for use in medium to long range (> 10 km) remote monitoring of nuclear reactors. These detectors utilize the coincident detection of the positron and neutron from the inverse beta decay (IBD) interaction ($\bar{\nu}_e + p \rightarrow n + e^+$)

to determine both the flux and energies of the incident antineutrinos. Water is an attractive option when scaling to such large detector sizes primarily due to both cost and environmental factors; and gadolinium is added (typically 0.1% by weight) to significantly increase both the neutron-tagging efficiency ($\sim 85\%$) and capture energy (~ 8 MeV). In this work, we analyze whether, in addition to the rate and energy, these detectors can determine the direction of the incident antineutrinos. Directional sensitivity might prove crucial in instances where multiple reactors are located nearby, or if a clandestine reactor has been confirmed via the IBD signal, directionality could be used in conjunction with other measurements, such as satellite imagery, to determine the location of the reactor. Once the location is known, other methods could be employed to further characterize the reactor.

Event-by-event reconstruction of the antineutrino direction via IBD in hydrogenous media requires knowledge of the neutron momentum vector within a few recoils following its production. This method of directional reconstruction has not yet been accomplished for reactor antineutrinos in any medium. In liquid scintillator detectors, CHOOZ [7] has shown that a partial and stochastic knowledge of the direction of an incoming antineutrino flux may be gained over time by reconstructing the relative positions of the positron and neutron thermal capture interaction vertices from an ensemble of IBD interactions. WCDs, however, presently do not possess the spatial resolution or sensitivity to do this. In this paper, we investigate whether an alternative interaction, elastic electron scattering (ES), can be used to determine the direction of a reactor antineutrino flux incident upon a WCD. The ES interaction ($\bar{\nu}_e + e^- \rightarrow \bar{\nu}_e + e^-$) is highly directional, meaning the electrons are primarily scattered

* Corresponding author; Email: dhellfeld@berkeley.edu; Tel.: +1 949 680 9345; Present address: Department of Nuclear Engineering, University of California, Berkeley, Berkeley, CA 94720.

† Second author; Email: dazeley2@llnl.gov; Tel.: +1 925 423 4792.

with a small scattering angle relative to the incident antineutrino. Thus, in principle, the direction of the incident antineutrino flux can be determined via directional reconstructions of an ensemble of scattered electrons.

A. Antineutrino-electron interactions

The elastic antineutrino-electron scattering cross-section including both the neutral and charged current components can be written as

$$\sigma(E_{\bar{\nu}_e}) = \left(\frac{G_F^2 m_e E_{\bar{\nu}_e}}{6\pi} \right) \left(1 + 2 \sin^2 \theta_w + 4 \sin^4 \theta_w \right) \approx (7.8 \times 10^{-45}) m_e E_{\bar{\nu}_e} \frac{\text{cm}^2}{\text{MeV}^2}, \quad (1)$$

where G_F is Fermi's coupling constant [$= 1.166364 \times 10^{-5} \text{ GeV}^{-2} (\hbar c)^3$] and θ_w is the Weinberg mixing angle ($\sin^2 \theta_w \approx 0.23$) [8]. Though the ES cross-section is much smaller than IBD, note that the nuclear reactor antineutrino flux is concentrated at low energies, where the interaction cross-section difference is smallest. Water also presents five times as many ES targets as IBD per water molecule ($10 e^-$ vs. 2 quasi-free protons) [see Fig. 1(a)].

From energy and momentum conservation in the laboratory frame, it can be shown that the kinetic energy of the scattered electron T_e , is given by

$$T_e = \frac{2m_e E_{\bar{\nu}_e}^2 \cos^2 \theta}{(m_e + E_{\bar{\nu}_e})^2 - E_{\bar{\nu}_e}^2 \cos^2 \theta}, \quad (2)$$

where θ is the angle between the incident antineutrino and the scattered electron [8]. Using this, the differential cross-section as a function of the cosine of the scattering angle can be expressed by

$$\frac{d\sigma}{d\cos\theta}(\theta, E_{\bar{\nu}_e}) = \frac{4\sigma_0 E_{\bar{\nu}_e}^2 M^2 \cos\theta}{M^2 - E_{\bar{\nu}_e}^2 \cos^2 \theta} \cdot \left[g_1^2 + g_2^2 - \left(\frac{2g_2^2 m_e E_{\bar{\nu}_e} \cos^2 \theta}{M^2 - E_{\bar{\nu}_e}^2 \cos^2 \theta} \right)^2 - \frac{2m_e^2 g_1 g_2 \cos^2 \theta}{M^2 - E_{\bar{\nu}_e}^2 \cos^2 \theta} \right], \quad (3)$$

where $\sigma_0 = 88.06 \times 10^{-46} \text{ cm}^2$, $M = m_e + E_{\bar{\nu}_e}$, $g_1 = \frac{1}{2}(g_V - g_A)$, and $g_2 = \frac{1}{2}(g_V + g_A)$ where g_V and g_A are the weak vector and weak axial-vector coupling constants, respectively [8]. The differential cross-section is plotted in Fig. 1(b) for several incident antineutrino energies. Due to the trend of the cross-section to increase towards $\cos\theta = 1$, the scattered electrons are primarily scattered in the direction of the incident antineutrinos. Note that the effect becomes more apparent as the incident antineutrino energy increases.

B. Reactor antineutrino energy spectrum

The fission of uranium and plutonium inside of nuclear reactor systems produce neutron-rich fission frag-

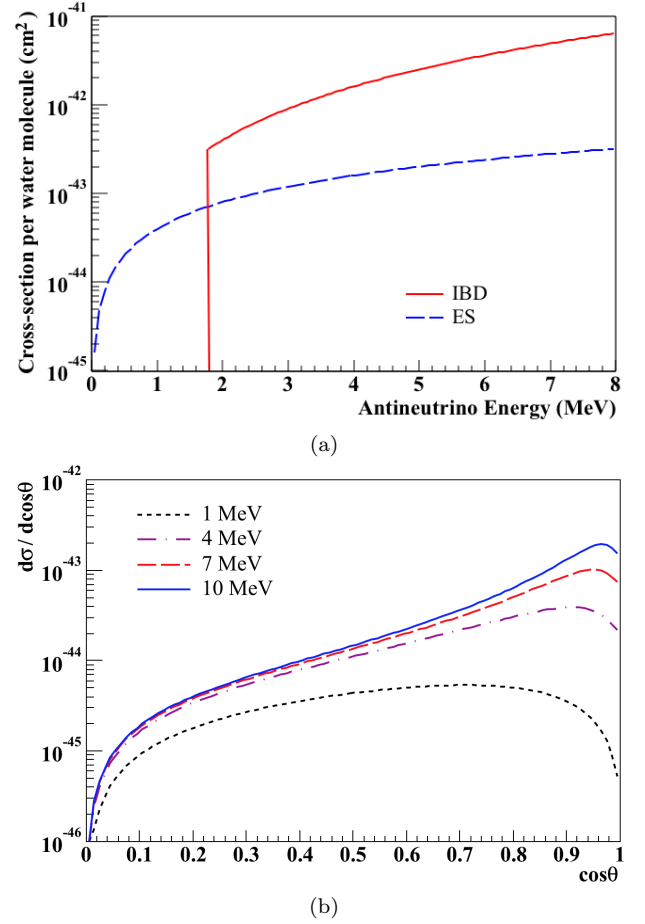


FIG. 1. (Color online) (a) ES and IBD cross-sections per water molecule as functions of incident antineutrino energy. Note the 1.8 MeV energy threshold for IBD. (b) Antineutrino-electron scattering differential cross-section as a function of the cosine of the scattering angle θ .

ment pairs, which beta decay six times on average before reaching stability. Each one of these decays will produce an antineutrino with a continuum of possible energies. Therefore, experiments and simulations are used to study both the production and subsequent decay of fission products in critical nuclear reactor systems to understand the reactor antineutrino energy spectrum. As shown by [9], the number of antineutrinos produced per fission per MeV can be modeled for a particular fissionable isotope by

$$\phi = \exp\left(\sum_{i=0}^2 a_i E_{\bar{\nu}_e}^i\right), \quad (4)$$

where the a_i parameters are specific to each isotope. Table I displays the fitted a_i values for the four most dominant fissioning isotopes ($> 99\%$ of all fissions) in nuclear reactors: ^{235}U , ^{238}U , ^{239}Pu , and ^{241}Pu . Though Eq. (4) and Table I were determined for reactor antineutrinos relevant to IBD interactions ($> 1.8 \text{ MeV}$), for the purpose of this work, it was assumed that Eq. (4) was valid

below this threshold.

TABLE I. Parameter values for Eq. (4). The values reported for ^{235}U , ^{239}Pu , and ^{241}Pu are for thermal neutrons and the value for ^{238}U is for 0.5 MeV neutrons [9].

Isotope	a_0	a_1	a_2
^{235}U	0.870	-0.160	-0.0910
^{238}U	0.976	-0.162	-0.0790
^{239}Pu	0.896	-0.239	-0.0981
^{241}Pu	0.793	-0.080	-0.1085

The isotopic fissioning concentrations in a nuclear reactor will depend on the reactor design as well as the level of fuel burnup. In this work, fission concentrations of a typical mid-cycle pressurized light water reactor (PWR) were used (49.6% ^{235}U , 35.1% ^{239}Pu , 8.7% ^{238}U , and 6.6% ^{241}Pu) [10]. The emitted antineutrino energy spectra per fission for each isotope as well as the summation of the four isotopes weighted by the typical PWR concentrations are plotted in Fig. 2 with dashed curves. As was mentioned before, reactor antineutrinos possess relatively low energies, with an average energy of about 1.5 MeV. Folding the incident antineutrino energy spectrum with the ES cross-section results in the observable/detectable spectrum shape in a detector. The detectable spectra per fission of the four isotopes as well as their weighted sum are plotted in Fig. 2 with solid curves. The average detectable reactor antineutrino energy is approximately 2 MeV.

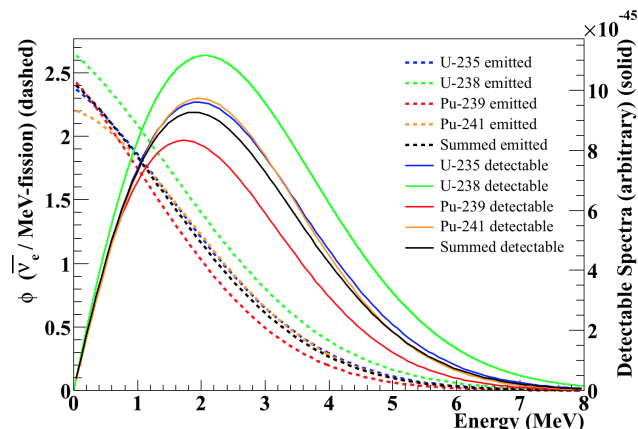


FIG. 2. (Color) Emitted (dashed) and detectable (solid) antineutrino energy spectra per fission from fissions occurring in ^{235}U , ^{239}Pu , ^{238}U , and ^{241}Pu . The black lines represent the summation of the four isotopes weighted by the typical fission concentrations of a mid-cycle PWR (49.6% ^{235}U , 35.1% ^{239}Pu , 8.7% ^{238}U , and 6.6% ^{241}Pu).

II. PROPOSED DETECTOR DESIGN

For this paper we begin by considering a detector design slightly modified from the recently proposed WATCHMAN project [6] - a kiloton scale WCD constructed from a large cylindrical stainless steel tank [see Fig. 3(a)]. The diameter and height of the cylinder are 15.8 m with a total water volume of about 3.1 kilotons. Photomultiplier tubes (PMTs) are housed in a cylindrical structure 13.8 m in diameter, separating the detector into two distinct regions. The outer region serves as a veto region for cosmic muons and the inner region as the target. There is approximately 2.1 kilotons of Gd-doped water in the target and 1 kiloton in the veto. The PMT support structure houses approximately 4300 30.48 cm (12 inch) Hamamatsu PMTs facing the target, with photocathode coverage near 40%, and 480 PMTs facing the veto. Within the target, a cylindrical fiducial volume (FV) was initially defined with a diameter and height of 10.82 m (~ 1 kiloton). The 1.5 m thick space between the PMT support structure and fiducial volume acts as a buffer region and enables better reduction of backgrounds from the PMTs and external radiation. The detector will be placed underground with 1500 meters of water equivalent (m.w.e.) overburden and approximately 13 km away from a single-core 3.758 GWt light water nuclear reactor as outlined in [6].

To model detector response, a GEANT4 [11] simulation package named Reactor Monitoring Simulation (RM-Sim) was used. RMSim is a modified version of WC-Sim [12], a GEANT4-based program for developing and simulating large WCDs. RMSim contains all relevant physics processes such as particle generation and transport, Cherenkov physics, optical photon production and transport, PMT sensitivity, digitization, and timing. Detailed detector geometry, materials, and optical properties for the WATCHMAN detector are also included. See Fig. 3(b) for a visualization of an antineutrino-electron scattering event in the simulated detector. Event reconstruction was handled by the fitter software code named BONSAI [13], originally developed for the Super Kamiokande (Super-K) experiment. We note that at the time of this writing, BONSAI was not yet optimally tuned to the specifications of the proposed detector.

Note that the WATCHMAN detector was not originally designed with ES directional sensitivity in mind. The WATCHMAN design was used as a baseline model here simply because a detailed GEANT4-based simulation already existed. In Sec. V A, modifications to the depth, size, and other features of the detector that improve ES directional sensitivity to the reactor antineutrino flux are considered.

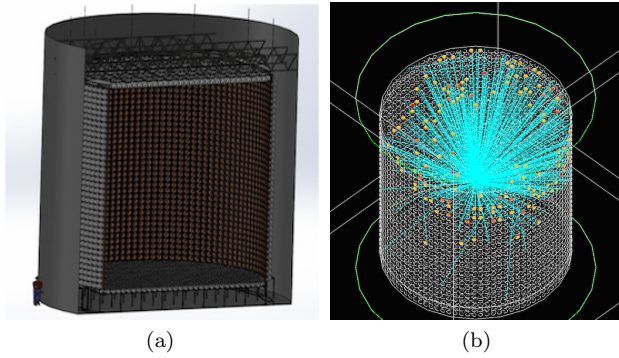


FIG. 3. (Color) (a) Basic design of the proposed kiloton WCD [6]. (b) Visualization of an ES event in the proposed detector modeled in RMSim. The blue lines represent the Cherenkov light and the colored dots represent triggered PMTs.

III. SIGNAL

The reactor-based elastic antineutrino-electron scattering rate in a detector can be determined using

$$R_{\bar{\nu}_e/e^-} = \frac{N_e}{4\pi d^2} \sum_i f_i \int \phi_i(E_{\bar{\nu}_e}) \sigma(E_{\bar{\nu}_e}) dE_{\bar{\nu}_e}, \quad (5)$$

where N_e is the number of available target electrons, d is the reactor-detector distance (cm), f_i is the fission rate for the particular isotope i (Hz), $\phi_i(E_{\bar{\nu}_e})$ is the number of antineutrinos produced per fission per MeV for isotope i [see Eq. (4)], and $\sigma(E_{\bar{\nu}_e})$ is the energy dependent scattering cross-section (cm^2) [see Eq. (1)]. The sum runs over the four dominant fissionable isotopes in nuclear reactors mentioned in Table I and the integral runs from 0 to 8 MeV, as in Fig. 2. Carrying out the calculation with the specifications outlined above results in about 9270 total scattering events in the kiloton FV over 5 years (not yet including detector response).

An elastic electron scattering generator was developed for RMSim to simulate the scattered electrons. The generator calculates the total number of expected interactions for any user provided detector size, acquisition time, standoff distance, reactor power level, and fission isotopics using Eq. (5). It then generates a sample of scattering events by sampling position, energy, and direction using Eqs. (2-4).

Five years worth of ES events were simulated in RMSim and reconstructed using the BONSAI fitter software. The reconstructed cosine of the scattering angles are shown in Fig. 4(a) with a value of $\cos \theta = 1$ denoting a complete forward scatter of the electron. The reconstructed distribution appears to follow an exponential-like distribution peaking at $\cos \theta = 1$. RMSim imposes a triggering threshold of 16 photoelectrons, and it can be seen from the plot that only 1550 ($\sim 17\%$) of the original 9270 ES events trigger the detector. Figure 4(b) shows the detector response of the triggered ES events for 5 years in terms of photoelectrons. The distribution

follows a decreasing exponential that extends to ~ 140 photoelectrons.

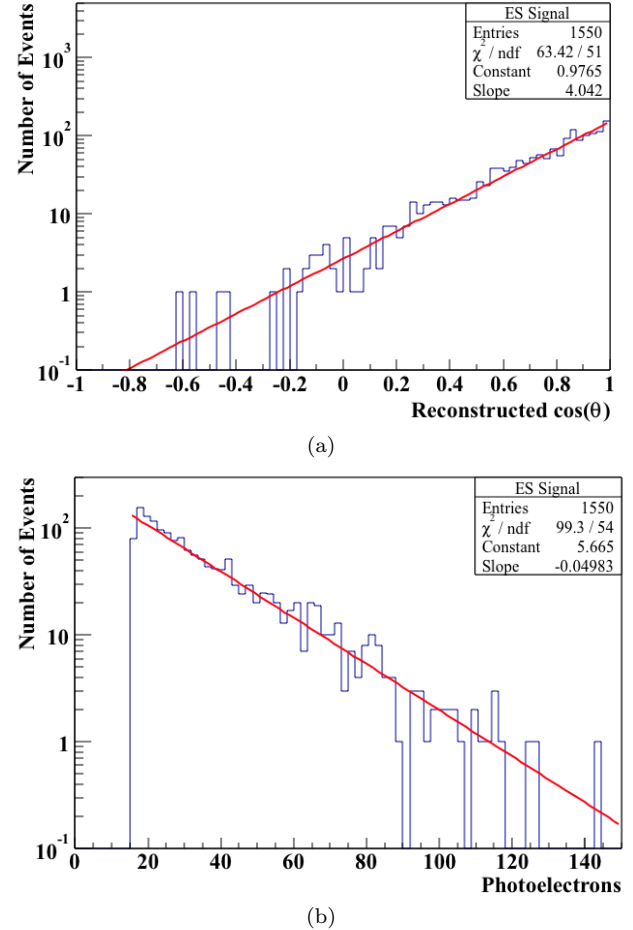


FIG. 4. (Color online) (a) Reconstruction of the cosine of the scattering angle distribution for 5 years of reactor ES in the proposed WCD. (b) Detected photoelectron distribution of the 5-year triggered signal.

IV. BACKGROUNDS

Due to the low count rates associated with antineutrino detection, the background levels in the detector must be kept to a minimum to maintain suitable statistics. Several potential sources of background exist for ES including cosmogenic radionuclides, high-energy gamma rays from the steel vessel and the rock surrounding the detector, solar neutrinos, misidentified IBD events from the reactor, PMT gamma rays, and water-borne radon. All were assumed to be distributed isotropically in direction (neglecting the obvious anisotropy of solar neutrinos). Therefore in a directional cosine plot, the ES signal [Fig. 4(a)] should appear as a peak in the forward direction atop a flat background.

A. Cosmogenic radionuclides

Cosmic muon spallation products can interact with the oxygen atoms in the target region water and create long-lived (> 1 s) radionuclides. If the nuclides beta decay in the inner detector region, the resultant electrons can trigger the PMTs and mimic the ES signal. The production yields of cosmogenic radionuclides have yet to be directly measured in water, thus a FLUKA study done by [14] on the 2700 m.w.e. deep Super-K detector was utilized. Table II displays the results for the five isotopes determined to be the most relevant for reactor antineutrino-electron scattering due to their long lifetimes and/or high yields.

The production yields in Table II are converted to production rates using

$$R_i = \rho Y_i L_\mu R_\mu, \quad (6)$$

where ρ is the density of the target (g cm^{-3}), Y_i is the yield of isotope i ($10^{-7} \mu^{-1} \text{g}^{-1} \text{cm}^2$), L_μ is the average muon path length in the detector (cm), and R_μ is the muon rate (Hz). To calculate the rates for the proposed detector (1 kiloton at 1500 m.w.e.), the muon rates and average path length were scaled appropriately from the Kamioka Liquid scintillator ANTineutrino Detector (KamLAND) experiment [15, 16], taking into account the different FV size and shallower depth. KamLAND values were used because they are readily available and the detector is at the same depth as Super-K (recall Table II is for cosmogenic radionuclide production at 2700 m.w.e.). To determine the scaling factor between the muon rates at 2700 m.w.e. and 1500 m.w.e., an existing GEANT4 simulation of muon flux as a function of depth and energy with a representative sea level muon energy spectrum was used [17]. The simulation predicted the showering and non-showering muon rates at 1500 m.w.e. to be about 2.2 and 5.3 times larger than at 2700 m.w.e., respectively.

The outer veto is used to identify and reject spallation events following muons entering the detector. For this work, an additional muon veto must be applied to reduce cosmogenic radionuclide decays. Following a muon that traverses the inner FV region, all events within 10 s and 2 m of a showering muon track, or within 10 s and 1 m of a non-showering muon track are removed. The detector live time (67%) was calculated conservatively assuming that all muons traverse the entire length of the cylindrical FV. In Sec. V A, modifications to the veto time to further reduce cosmogenic radionuclide events are considered.

Table III shows the estimated backgrounds due to cosmogenic radionuclides over the period of 5 years in the 1000 m^3 FV accounting for the position sensitive veto and 67% live time (not including the 16 photoelectron threshold). Due to its long lifetime and large yield, ^{16}N significantly dominates the mix. Uncertainties in the vertex reconstruction, which results in some radionuclide events being reconstructed outside the tubular veto regions surrounding the muon tracks, also contributed. The likelihoods of such events were determined via independent simulations and included in the table.

Some of the cosmogenic radionuclides of Table III, including ^{16}N , beta decay into an excited state, resulting in the simultaneous emission of a gamma ray. These gamma rays can, via either the photoelectric effect, Compton scattering, or pair production, produce Cherenkov emitting, high-energy electrons. Since the fitter software searches for a single Cherenkov cone in each event, the presence of two cones tends to increase the uncertainty of the reconstruction. This can be used to discriminate these types of events from the ES signal. For example, Fig. 5 shows the log likelihood parameter (a measure of the goodness of fit) for the reconstructed events against the number of triggered PMTs for both ^{16}N and ES events. From the plot, the ES events create a narrow, almost proportionate, band (shown in red), whereas the ^{16}N events (shown in blue) follow a similar behavior but with a large grouping of events with lower log likelihood. This is due to the 6.1 MeV gamma ray being emitted coincident with the beta decay. These events can be discarded while keeping all of the ES events by applying a simple cut to any events that fall above the green line ($y = 0.39x + 27$) in Fig. 5. In doing so, roughly 46% of the ^{16}N background events are removed.

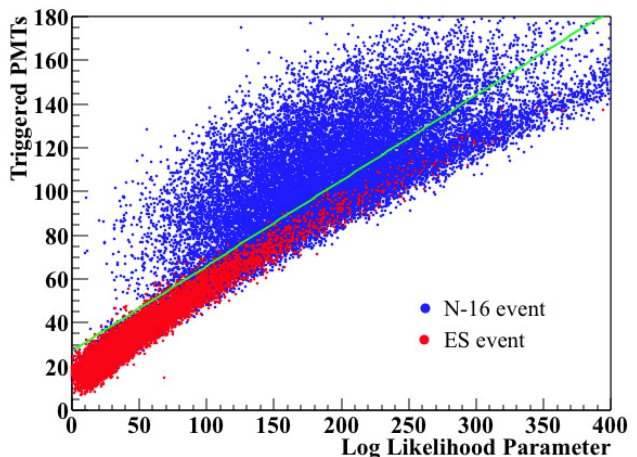


FIG. 5. (Color) The number of triggered PMTs as a function of the log likelihood of ES and ^{16}N fits. Events above the green line ($y = 0.39x + 27$) are due to a gamma ray being emitted in coincidence with the ^{16}N beta decay and can be removed.

B. PMT gamma rays

The PMT glass will contain trace amounts of natural U, Th, and K. The decays of ^{208}Tl (from the Th decay chain) and ^{40}K will produce 2.6 MeV and 1.4 MeV gamma rays, respectively. Most of these will interact outside the FV, but due to the uncertainty in the event reconstruction, some events will be reconstructed inside, contributing to the background. An arbitrary number of PMT gamma rays were simulated in RMSim and the

TABLE II. FLUKA simulation results of cosmogenic radionuclide production in the Super-K detector done by [14]. Only the isotopes determined to be relevant to reactor antineutrino-electron scattering are considered.

Isotope	Half-life (s)	Decay Mode	Yield ($10^{-7} \mu^{-1} \text{g}^{-1} \text{cm}^2$)	Leading Production Process (on ^{16}O)
^{16}N	7.13	$\beta^- \gamma$ (66%), β^- (34%)	18	(n, p)
^{15}C	2.45	$\beta^- \gamma$ (63%), β^- (37%)	0.8	$(n, 2p)$
^{11}Be	13.8	β^- (55%), $\beta^- \gamma$ (45%)	0.8	$(n, \alpha + 2p)$
^8B	0.77	β^+	5.8	$(\pi^-, \alpha + 2p + 2n)$
^8Li	0.84	β^-	13	$(\pi^-, \alpha + {}^2\text{H} + p + n)$

TABLE III. Estimated background events due to cosmogenic radionuclides at a depth of 1500 m.w.e. over a period of 5 years in the 1000 m^3 FV with a 10 second position sensitive veto system and 67% live time (16 photoelectron threshold not included).

^{16}N	^{15}C	^{11}Be	^8B	^8Li	Total
36077	326	514	768	1436	41121

black curve (right diagonal shading) in Fig. 6 shows the distance from the reconstructed interaction vertex to the nearest PMT for each event. From the figure, it is clear that a significant number of events are reconstructed inside the FV (> 150 cm away from the PMTs), forming two distinct groups. Near the PMTs, the black curve appears to follow an exponential, whereas further away from the PMTs an almost flat distribution is observed. To improve upon the results, we attempt to remove the poorly fit events. By applying a cut to the log likelihood parameter (≥ 25) and the number of triggered PMTs (≥ 25), roughly half of the events are removed, leaving an exponential distribution with respect to the distance to the PMTs (shown in blue and left diagonal shading in Fig. 6).

The exponential behavior of the blue curve (left diagonal shading) in Fig. 6 is a promising result, if realizable in practice. It implies that the PMT gamma ray background can be reduced to a subdominant level with a large enough buffer region. To reduce the PMT gamma ray backgrounds with a fixed detector size however, the FV must be decreased to allow for a sufficient buffer thickness. This will result in a significant reduction in the number of detectable ES interactions. Assuming an exponential distribution with respect to distance from the PMTs, the PMT gamma-ray background can be estimated for any sized FV using the assumed impurity levels of Th and ^{40}K in the glass. In this work, the PMTs are assumed to have similar radioactivity levels as the low-background 25.4 cm (10 inch) Hamamatsu PMTs employed at the Double CHOOZ detector with Th and ^{40}K impurity concentrations of 0.03 ppm and 20 ppm, respectively [18].

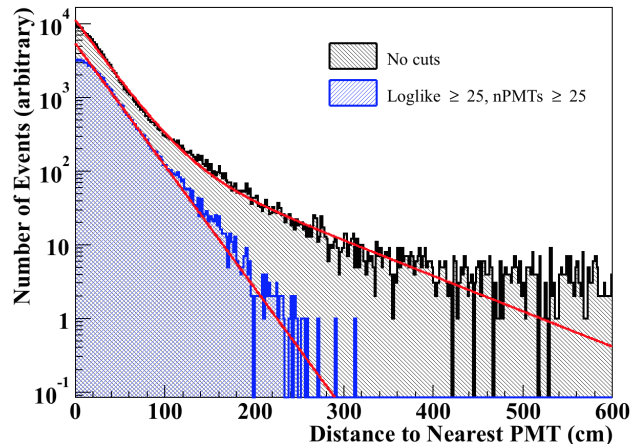


FIG. 6. (Color online) PMT-based background events as a function of the distance from the reconstructed vertex to the nearest PMT (black and right diagonal shading). The blue curve (left diagonal shading), which requires both the triggered PMT count (nPMTs) and the log likelihood (Loglike) to be ≥ 25 , follows an exponential distribution.

C. Water-borne $^{222}\text{Rn}/^{214}\text{Bi}$

The beta decay of ^{214}B (a daughter product of the ^{238}U decay chain product ^{222}Rn , $Q = 3.3$ MeV) in the target region will also contribute a significant amount of background to the ES signal. The presence of $^{222}\text{Rn}/^{214}\text{Bi}$ in the water can occur due to a variety of processes. Some may result due to trace amounts of naturally occurring ^{238}U present in the water, dissolved ^{222}Rn that has migrated out of the PMT glass, and from radon gas entering the detector from the mine air. The Sudbury Neutrino Observatory (SNO) heavy water neutrino detector has reported an inner detector radon contamination of 10^{-14} gU/gD $_2$ O, assuming the U is in secular equilibrium with ^{222}Rn [19]. Assuming this level of contamination in the proposed light water detector results in about about 10^4 ^{214}Bi decays per day somewhere in the 1000 m^3 FV, of which approximately 20% survive the GEANT4 detector simulation trigger condition (16 photoelectrons). If 67% live time is assumed, approximately 1350 events per day can be expected ($\sim 2.4 \times 10^6$ in 5 years).

Actual radon levels achievable in a real detector will

rely on the water recirculation methods employed, as well as the radon concentration in the mine air, both of which could be significantly different than SNO. The SNO detector also employs an acrylic barrier between the heavy water target and the light water buffer. The acrylic, while it impedes the migration of radon from the PMTs to the target, might also be a mild source of radon. One might envision a different water flow scheme, in which radon free fresh water is injected inside the target and directed outward via positive pressure through a permeable acrylic barrier, which could achieve a reduction in radon contamination relative to SNO. In this work, since it is difficult to predict physically achievable radon concentrations, we begin simply by assuming similar concentrations to SNO, and later investigate hypothetical situations in which the radon contamination can be reduced further.

D. Other backgrounds

The backgrounds due to gamma rays from the detector steel vessel and the surrounding rock were determined using a study performed by the Isotope Decay At Rest (IsoDAR) collaboration on the KamLAND detector [20]. IsoDAR assumed a 5 m sphere FV at KamLAND, thus the results from [20] were scaled to account for the much larger cylindrical FV of the proposed detector (1000 m^3). Specifically, the estimates were scaled using the difference in the fiducial surface areas. This method assumes the proposed detector steel vessel will have similar cleanliness levels as KamLAND and the surrounding rock will be of similar composition to the KamLAND mine. The differences in densities and gamma attenuation lengths between the scintillator used in KamLAND and the water used in the detector under study, as well as the differences in gamma path lengths for the spherical and cylindrical geometries were neglected. All gamma rays that reached the FV were assumed to interact.

The ^8B solar neutrino background was also determined by scaling from [20]. Assuming the neutrino flux will not differ between the KamLAND depth (2700 m.w.e.) and the depth proposed here (1500 m.w.e.), the interaction rate is dependent solely on the number of available targets, which is proportional to the fiducial mass. Therefore the solar neutrino background estimation in [20] was scaled according to the difference in the KamLAND fiducial mass (0.408 kilotons) and the proposed detector fiducial mass (1 kiloton).

The scaled steel, rock, and solar neutrino results from [20] were corrected for the difference in detector live time between KamLAND (56.2%) and the proposed detector (67%). Corrections were also included to account for the 3 MeV visible energy threshold used in [20].

If the neutron from a reactor-based IBD event is not detected within the time or spatial coincidence requirements, or it is simply not captured, then the lone positron signal will mimic ES. These misidentified IBD back-

grounds were estimated assuming an IBD interaction rate of 20 events per day and a 20% missed neutron rate as in [6].

V. ANALYSIS

As mentioned in Sec. IV, background events are assumed to be isotropic in direction. Reconstructed ES signal events exhibit an exponential behavior towards $\cos\theta = 1$. Therefore, in a plot of the cosine of the scattering angle, we expect the total signal to follow the behavior of a constant plus an exponential curve as in

$$y = A + Be^{Cx}, \quad (7)$$

where A , B , and C are free parameters in the fit to the data. To determine the statistical significance of the ES signal, an arbitrarily large independent sample of ES events was simulated to determine the exponential slope parameter C . With the slope parameter fixed, the uncertainty in the exponential normalization parameter B was used to determine the uncertainty and statistical significance of the signal. This analysis method would only be possible in practice if the exponential slope could be obtained *a priori* using directional calibrations, such as the electron accelerator at Super-K [21].

Fig. 7 displays the detector response (photoelectron production) from all sources of backgrounds as well as the ES signal for a time period of one year in the kiloton detector at 1500 m.w.e. From the plot it is clear that the radionuclides, PMTs, and $^{222}\text{Rn}/^{214}\text{Bi}$ dominate the total number of backgrounds.

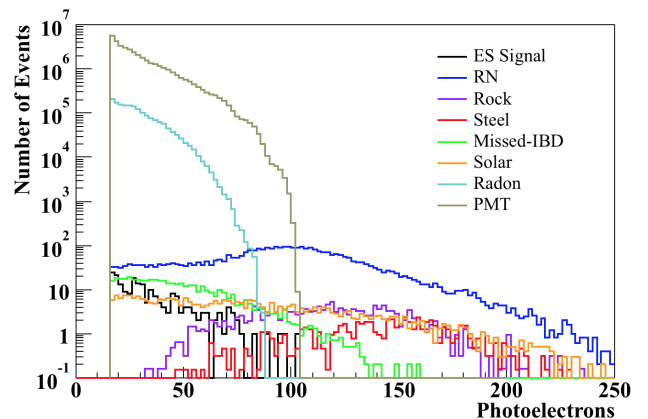


FIG. 7. (Color) The most significant backgrounds expected in the kiloton FV over a one-year data acquisition period together with the ES signal. PMT gamma rays, water-borne $^{222}\text{Rn}/^{214}\text{Bi}$ and cosmogenic radionuclides represent the three most important background types shown here. In the following, promising techniques for reducing many of these backgrounds to a subdominant level are investigated.

We now investigate methods to remove background while retaining as much ES signal as possible. First, note

that the PMT and radon based backgrounds are more heavily concentrated at low energies than the ES signal. We can therefore look to higher energy events to remove PMT and radon based backgrounds without removing too much signal. The radionuclide background, however, dominates at higher energies. Therefore the sensitivity of relatively small slices in the higher energy domain ($50 \rightarrow 80$ and $60 \rightarrow 90$ triggered PMTs) was investigated. At higher energies, the PMT based backgrounds are both lower in number and more accurately reconstructed, and thus larger FVs can be used. For the radon, it is clear that a significant improvement in radon contamination (over the SNO levels) would need to be made before ES directionality might be achievable. We cannot comment on whether a dedicated R&D campaign, or a new scheme of optimized water flow might be able to achieve significant improvements. Here we simply assume significant reductions (by factors 10^{-2} and 10^{-4}) and calculate the sensitivities that result.

In addition to the high energy slices, a wider slice in the lower energy domain ($25 \rightarrow 65$ triggered PMTs) was used in an effort to retain more ES signal. This slice will only become practical in the instance where the radon levels as well as the FV are significantly reduced. Table IV displays the individual and total background estimates for the three different analysis cuts. For each slice, the table also displays the expected number of ES signal events and the fixed exponential slope used in Eq. (7). Finally, the average statistical significance (the mean significance of repeated trials) was calculated for the different assumed levels of radon in the detector. The results presented here were determined with respect to an assumed known antineutrino direction.

Average statistical significances of about 3σ may be achieved with the $25 \rightarrow 65$ slice if the radon levels can be reduced by four orders of magnitude from SNO. If radon cannot be reduced to that degree, then the higher energy slices will have to be utilized. In this case, further background reduction techniques must be utilized to produce a significant signal.

A. Sensitivity vs. depth

As shown in the previous section, cosmogenic radionuclide decays become the dominant background contributor at higher energies. We therefore investigate how the directional sensitivity can be improved if the proposed detector is placed deeper underground with a greater overburden. To do so, we first determine how the showering and non-showering muon rates scale with depth using the muon simulation mentioned in Sec. IV A. The results of the simulation (relative to the KamLAND depth) are shown in Fig. 8(a).

Using the muon scalings, the radionuclide background and detector live time were determined as a function of depth. Because the muon rate decreases significantly with depth, the position sensitive veto time can be in-

creased to remove more radionuclide background without suffering any live time losses. Therefore, as the depth is increased, the 10 s veto time is increased to maintain a constant 67% live time. A maximum veto time of 20 s was set to prevent giving the radionuclides enough time to migrate outside of the tubular veto. Figure 8(b) displays the veto times and detector live times as a function of depth used in subsequent calculations. A veto time of 20 s is reached at 2100 m.w.e. and remains fixed at deeper depths.

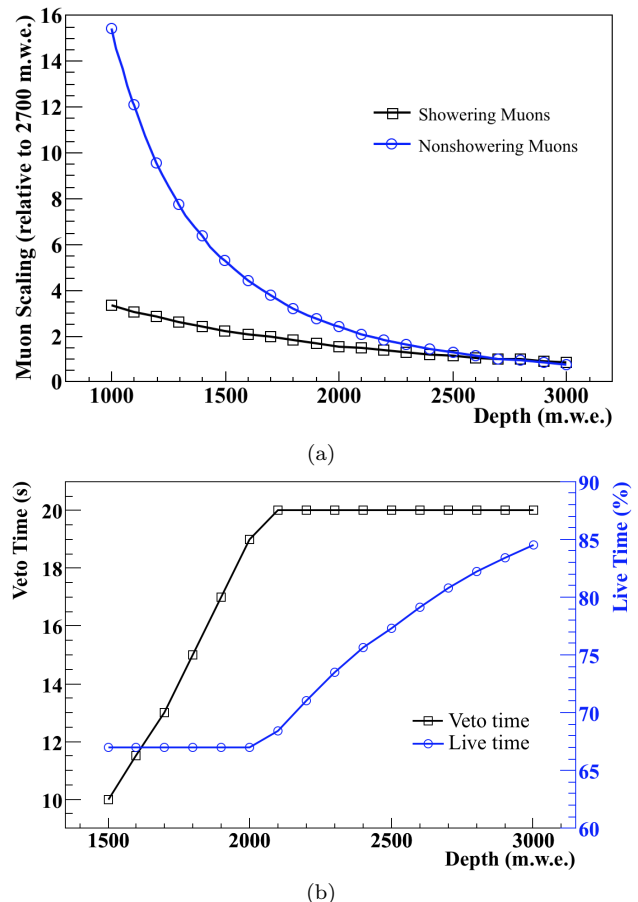


FIG. 8. (Color online) (a) Showering and non-showering muon rates as a function of depth (relative to KamLAND) determined from a GEANT4 simulation [17]. (b) Veto times used in the position sensitive veto system as a function of depth and the resultant detector live times. The veto time was increased as a function of depth from 10 s at 1500 m.w.e. in order to retain a 67% live time. A maximum veto time was set at 20 s, which was reached at 2100 m.w.e.

The average statistical significances as a function of depth and radon contamination relative to SNO were then determined. Only the $25 \rightarrow 65$ and $60 \rightarrow 90$ slices are included in the analysis to demonstrate the difference between the low and high energy domains. The results are shown in Fig. 9 for radon levels of $1 \times \text{SNO}$ [Fig. 9(a)], $10^{-2} \times \text{SNO}$ [Fig. 9(b)], and $10^{-4} \times \text{SNO}$ [Fig. 9(c)]. As mentioned in Sec. V, repeated multiple independent data

TABLE IV. Signal and background estimates for 5 years assuming three different energy analysis cuts. Average significances were calculated assuming the radon levels relative to those of SNO. The radionuclide background is denoted by “RN” and the backgrounds due to steel, rock, misidentified IBD, and solar neutrinos are combined together and denoted by “Other”. Since the ideal FV can change with increasing energy, we include the range of FVs used within each energy slice.

PMT Triggers	FV (m ³)	ES	Exp. Slope	RN	PMTs	Other	Radon (x SNO)		
							1	10 ⁻²	10 ⁻⁴
25 → 65	187	80	4.6	741	1212	438	638670	6387	64
Total Background Significance							641061	8778	2455
							0.2σ	1.6σ	2.9σ
50 → 80	400 - 500	48	6.0	1717	906	735	125430	1254	13
Total Background Significance							128788	4612	3371
							0.3σ	1.5σ	1.8σ
60 → 90	500 - 1000	43	6.7	3947	227	1171	34390	344	3
Total Background Significance							39735	5689	5348
							0.5σ	1.3σ	1.4σ

samples were used to calculate the mean significance per 5 year experiment. Error bars are included in the plots and represent the uncertainty in the mean, however are too small to be observed in most cases. The results from each single experiment form a Gaussian distribution with a width of approximately 1σ . Therefore, if a single physical experiment was performed to replicate one of the scenarios in the figure, there would be a 68% probability of reproducing the reported significance $\pm 1\sigma$. With no reduction in radon (relative to SNO), directionality does not seem to be possible at any depth with the current sized detector. As was mentioned above, as the radon contamination is significantly reduced (by four orders of magnitude), the 25 → 65 slice produces the most significant signal. This is clearly observed in Fig. 9(c), where a 3σ significance can be obtained using this slice starting at about 1500 m.w.e.

Finally, the effect of increasing the total detector size (including the fiducial, buffer, and veto) to obtain more ES signal was considered. For the three radon levels in Fig. 9(a)-(c), the required FV to produce a statistical significance of 3σ in each energy regime was determined. This was done assuming both the signal and background scale linearly with the FV, while significance scales with the signal (S) to background (B) ratio ($\frac{S}{\sqrt{B}}$). The respective buffer and veto thicknesses for each energy range were then added to determine the total detector size. The results are shown in Fig. 9(d)-(f) for all three radon levels. Error bars are included and represent the uncertainties in Fig. 9(a)-(c) propagated through the calculation. However, once again, the error bars represent the uncertainty in the mean and do not represent the uncertainty of a single experiment. In the instance where radon levels cannot be reduced, the detector size needs to be increased significantly (> 40 kilotons) in order for directionality to be possible. If significant radon reduction is possible, detector sizes anywhere from 3 to 10 kilotons may be sensitive to directionality, depending on the specific depth

and radon contamination.

All of the results shown here stem from a standardized assumption that the detector is placed 13 km away from a 3.758 GWt nuclear reactor. Both detector stand-off and reactor power level will affect the amount of signal seen by the detector and although not presented here, a study could be done to determine their effects on directional sensitivity. Finally, we reiterate that the results presented in Fig. 9 reflect a data acquisition period of 5 years. The IAEA timeliness detection goals can range from 1 to 12 months, depending on the material of interest [22], and thus directional measurements such as these would only have relevancy where it is necessary to check that the directional flux is consistent over the long term with the more time sensitive IBD signal.

VI. CONCLUSIONS

The preliminary results of this investigation suggest that reactor antineutrino directionality in a Gd-doped WCD placed approximately 10 km away from a commercial nuclear reactor will indeed be difficult, however under certain conditions, it may in fact be an achievable goal. With no progress in radon reduction (relative to SNO), the only hope for directionality is if a much larger detector is used (> 40 kilotons). With a moderate reduction in radon ($10^{-2} \times \text{SNO}$), directional sensitivity can be achieved using a combination of a larger detector and greater overburden. Finally, if a significant reduction in radon is possible ($10^{-4} \times \text{SNO}$), a 3 kiloton detector at 1500 m.w.e. (such as the proposed WATCHMAN detector) should be directionally sensitive. Inherent in these conclusions are the additional assumptions: similar steel cleanliness levels to the KamLAND detector, a continuously operated reactor at full power with no shutdown periods, and constant fission fractions that of a typical mid-cycle PWR. Also, the situation investigated here is

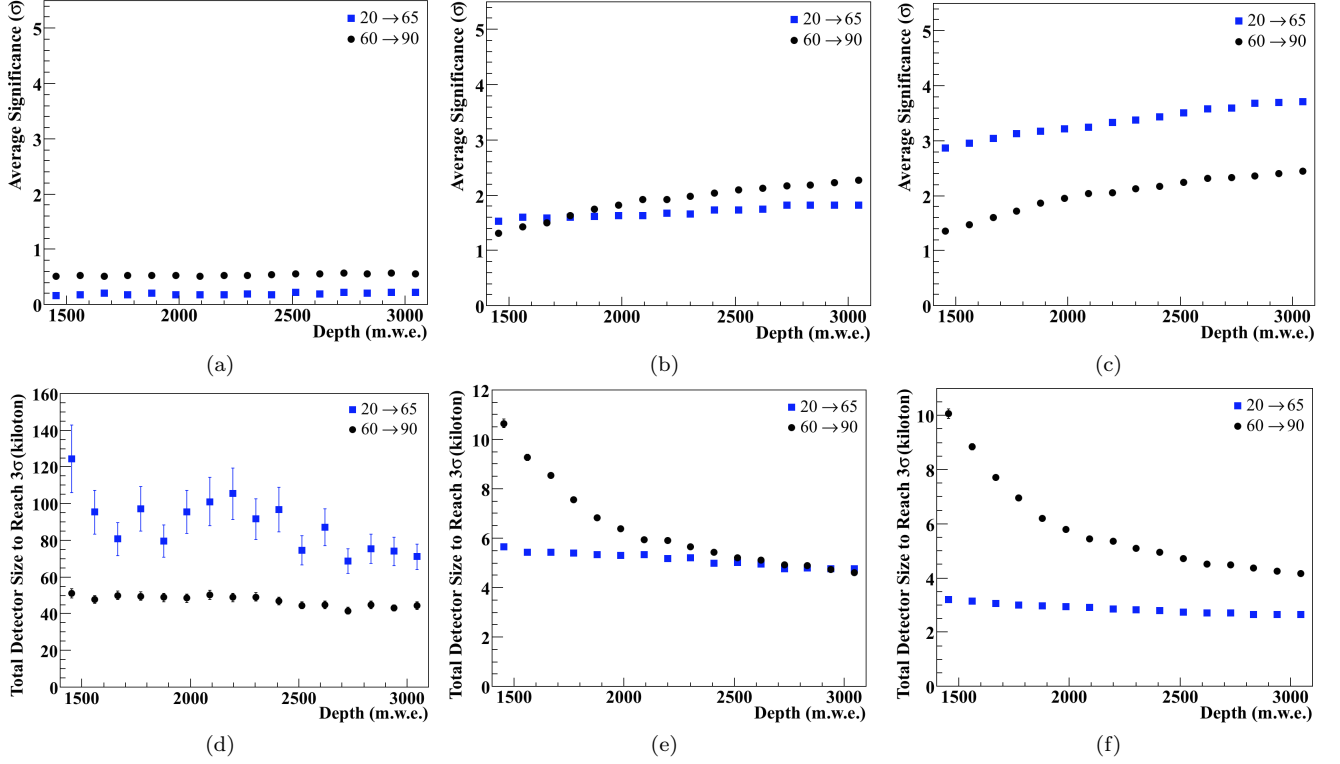


FIG. 9. (Color) Average statistical significance plotted as a function of depth using two different analysis cuts on the number of triggered PMTs, with radon levels of $1 \times \text{SNO}$ (a), $10^{-2} \times \text{SNO}$ (b), and $10^{-4} \times \text{SNO}$ (c). Error bars are included and represent the uncertainty in the mean (however they are too small to be observed in most cases). The uncertainty in a single experiment is about $\pm 1\sigma$. Total detector size required for 3σ significance plotted as a function of depth for radon levels of $1 \times \text{SNO}$ (d), $10^{-2} \times \text{SNO}$ (e), and $10^{-4} \times \text{SNO}$ (f). Again, error bars represent the uncertainty in the mean and do not represent the uncertainty in a single experiment. Therefore the results should only be used as a guide.

the directional sensitivity of an incoming antineutrino flux with respect to an assumed reactor location. If the true location is unknown, a statistical penalty would need to be applied for testing in multiple directions. While these conditions may be difficult to achieve in practice, we have demonstrated that Gd-doped WCDs may indeed possess the potential to utilize elastic electron scattering for nuclear reactor antineutrino directionality and thus further research in this topic may be warranted.

Ultimately, the most pressing condition that will affect directional sensitivity in Gd-doped WCDs is the ability to significantly reduce the radon contamination in the inner detector volume. If progress has been slow in this regard since the construction of the SNO detector, we hope that this research may serve as a catalyst to pursue an extensive R&D effort into water-borne radon removal techniques for future large scale Gd-doped WCDs used for remote monitoring of nuclear reactors.

ACKNOWLEDGEMENTS

The authors would like to thank Marc Bergevin of Lawrence Livermore National Laboratory for his help with the development and usage of RMSim for the purposes of this work and Michael Smy of the University of California, Irvine for his assistance with the BONSAI fitter software. This work was supported by the U.S. Department of Energy National Nuclear Security Administration under Award No. DE-NA0000979 through the Nuclear Science and Security Consortium, and Lawrence Livermore National Laboratory under Contract No. DE-AC52-07NA27344, release number LLNL-JRNL-679610. The views and opinions of authors expressed herein do not necessarily state or reflect those of the United States Government or any agency thereof.

[1] N. Bowden *et al.*, Nucl. Instrum. Methods A **572**, 985 (2007).

[2] L. Mikaelyan, in *Proceedings of the International Conference "Neutrino 77"*, Vol. 2 (Nauka, Moscow, 1978) pp.

- 383–385.
- [3] A. Bernstein, N. Bowden, A. Misner, and T. Palmer, J. Appl. Phys. **103**, 074905 (2008).
 - [4] A. Bernstein, G. Baldwin, B. Boyer, M. Goodman, J. Learned, J. Lund, D. Reyna, and R. Svoboda, Science & Global Security **18**, 127 (2010).
 - [5] T. Lasserre, M. Fechner, G. Mention, R. Reboulleau, M. Cribier, A. Letourneau, and D. Lhuillier, arXiv:11011.3850 (2010).
 - [6] A. Bernstein *et al.*, arXiv:1502.01132 (2015).
 - [7] M. Apollonio *et al.*, Phys. Rev. D **61**, 012001 (1999).
 - [8] C. Giunti and C. Kim, *Fundamentals of Neutrino Physics and Astrophysics* (Oxford University Press, Oxford, 2007).
 - [9] P. Vogel and J. Engel, Phys. Rev. D **39**, 3378 (1989).
 - [10] G. Zacek *et al.*, Phys. Rev. D **34**, 2621 (1986).
 - [11] S. Agostinelli *et al.*, (GEANT4 Collaboration), Nucl. Instrum. Methods A **506**, 250 (2003).
 - [12] The Water Cherenkov Simulator (WCSim). Repository: <https://github.com/WCSim>.
 - [13] M. Smy, in *Proceedings of the International Cosmic Ray Conference*, Vol. 5 (HE part 2) (Mexico City, Mexico, 2008) pp. 1279–1282.
 - [14] S. Li and J. Beacom, Phys. Rev. C **89**, 045801 (2014).
 - [15] S. Abe *et al.*, Phys. Rev. C **84**, 035804 (2011).
 - [16] S. Abe *et al.*, Phys. Rev. C **81**, 025807 (2010).
 - [17] D. Reyna, arXiv:0604145v2 (2006).
 - [18] J. Felde, (private communication), Internal LBNE DocDB document number 729-v1 (2010).
 - [19] I. Belvis *et al.*, Nucl. Instrum. Methods A **517**, 139 (2004).
 - [20] J. Conrad, M. Shaevitz, I. Shimizu, J. Spitz, M. Toups, and L. Winslow, Phys. Rev. D **89**, 072010 (2014).
 - [21] Y. Koshio, Ph.D. thesis, University of Tokyo (1998).
 - [22] *IAEA Safeguards Glossary*, International Nuclear Verification Series 3 (The International Atomic Energy Agency, 2003).